Experimental and theoretical study of temperature dependent exciton delocalization and relaxation in anthracene thin films

Tai-Sang Ahn, Astrid M. Müller, and Rabih O. Al-Kaysi
Department of Chemistry, University of California, Riverside, California 92521, USA

Frank C. Spano
Department of Chemistry, Temple University, Philadelphia, Pennsylvania 19122, USA

Joseph E. Norton
School of Chemistry and Biochemistry, Georgia Institute of Technology, Atlanta, Georgia 30332-0400, USA and Center for Organic Photonics and Electronics, Georgia Institute of Technology, Atlanta Georgia 30332-0400, USA

David Beljonne
School of Chemistry and Biochemistry, Georgia Institute of Technology, Atlanta, Georgia 30332-0400, USA, Center for Organic Photonics and Electronics, Georgia Institute of Technology, Atlanta, Georgia 30332-0400, USA, and Laboratory for Chemistry of Novel Materials, University of Mons-Hainaut, B-7000 Mons, Belgium

Jean-Luc Brédas
School of Chemistry and Biochemistry, Georgia Institute of Technology, Atlanta, Georgia 30332-0400, USA and Center for Organic Photonics and Electronics, Georgia Institute of Technology, Atlanta, Georgia 30332-0400, USA

Christopher J. Bardeen[a)]
Department of Chemistry, University of California, Riverside, California 92521, USA

(Received 17 September 2007; accepted 14 November 2007; published online 6 February 2008)

The spectroscopy of solid anthracene is examined both experimentally and theoretically. To avoid experimental complications such as self-absorption and polariton effects, ultrathin polycrystalline films deposited on transparent substrates are studied. To separate the contributions from different emitting species, the emission is resolved in both time and wavelength. The spectroscopic data are interpreted in terms of a three-state kinetic model, where two excited states, a high energy state 1 and a low energy state 2, both contribute to the luminescence and are kinetically coupled. Using this model, we analyze the spectral lineshape, relative quantum yield, and relaxation rates as a function of temperature. For state 1, we find that the ratio of the 0-0 vibronic peak to the 0-1 peak is enhanced by roughly a factor of 3.5 at low temperature, while the quantum yield and decay rates also increase by a similar factor. These observations are explained using a theoretical model previously developed for herringbone polyacene crystals. The early-time emission lineshape is consistent with that expected for a linear aggregate corresponding to an edge-dislocation defect. The results of experiment and theory are quantitatively compared at different temperatures in order to estimate that the singlet exciton in our polycrystalline films is delocalized over about ten molecules. Within these domains, the exciton's coherence length steadily increases as the temperature drops, until it reaches the limits of the domain, whereupon it saturates and remains constant as the temperature is lowered further. While the theoretical modeling correctly reproduces the temperature dependence of the fluorescence spectral lineshape, the decay of the singlet exciton appears to be determined by a trapping process that becomes more rapid as the temperature is lowered. This more rapid decay is consistent with accelerated trapping due to increased delocalization of the exciton at lower temperatures. These observations suggest that exciton coherence can play an important role in both radiative and nonradiative decay channels in these materials. Our results show that the spectroscopy of polyacene solids can be analyzed in a self-consistent fashion to obtain information about electronic delocalization and domain sizes. © *2008 American Institute of Physics*.
[DOI: 10.1063/1.2822310]

INTRODUCTION

Understanding the electronic behavior of conjugated organic materials is a goal of both practical and fundamental importance. In principle, molecular crystals provide the simplest chemical system in which to study electronic phenomena such as intermolecular exciton formation and relaxation.[1] They can be grown with high chemical purity, and their molecular-level packing can be known to high precision through x-ray diffraction studies.[2] Recent work has centered on understanding the ultrafast dynamics of exciton relaxation

[a)]Electronic mail: christopher.bardeen@ucr.edu.

and charge generation in polyacene molecular crystals.[3,4] But while the electronic dynamics are being characterized, the nature of the states involved is often unclear. For example, the primary excited state is usually assumed to be a Frenkel exciton, but issues such as electronic wavefunction delocalization, phonon coupling, and the role of defects must be resolved in order to quantitatively model electronic processes that involve this state, such as charge separation. A sensitive probe of excited state structure is the spectral shape and decay rate of its luminescence. Perhaps the most thoroughly studied molecular crystal is anthracene, where several investigators did pioneering work in calculating its Frenkel exciton band structure.[5–8] Despite the theoretical results, the unequivocal observation of luminescence that can be assigned to the intrinsic exciton state of anthracene has been elusive.[9] One problem is that neither experimental measurements nor the theoretical description of the spectroscopy have been sufficiently detailed to permit quantitative comparison of experiment and theory.

Recent progress in both the experimental and theoretical understanding of molecular aggregates such as pseudoisocyanine dye *J* aggregates[10–12] and the biological light-harvesting complex[13–19] (LHC) has resulted in new insights into the mechanisms of exciton delocalization and dynamics. Unfortunately, transferring these insights to organic molecular crystals is not completely straightforward for several reasons. First, there exist several experimental challenges. *J* aggregates and LHC's suspended in aqueous solution are randomly oriented and much smaller than the wavelength of the exciting light. Thus all the standard spectroscopic tools used to study molecules in dilute solutions may be applied to these aggregate systems as well. Macroscopic molecular crystals, on the other hand, are prone to artifacts such as self-absorption, waveguiding, and polariton effects that make the measurement of even simple quantities such as the absorption spectrum challenging. A recent example of this is the wide range of literature values for the true magnitude of the Davydov splitting in crystalline α-sexithiophene.[20] In addition to optical artifacts, molecular crystals are also plagued by the presence of defect, surface states, and impurity molecules. The ability of excitons to rapidly diffuse through the crystal can lead to trapping, and the steady state luminescence may reflect the characteristics of these trap states as well as that of the initially created singlet exciton. Lastly, the practical challenges of doing spectroscopic measurements on molecular crystal systems are complemented by conceptual challenges in the interpretation of the spectra. Most models of the exciton structure in *J* aggregate and LHC systems assume a set of coupled two-level systems, with the inter- and intramolecular vibrations treated as a stochastic bath or similar line-broadening function.[19,21–25] In porphyrin and pseudoisocyanine aggregates, this approach may be justified by the absence of clear vibronic progressions in the absorption and emission spectra. This is not the case for most conjugated organic molecular crystals, where the lineshapes usually reflect the strong influence of intramolecular double bond motions in the frequency range of 1000–1500 cm^{-1}. The need to explicitly take the intramolecular vibrations into account in order to quantitatively model the lineshape has led to the extension and improvement of previous models for aggregate lineshapes.[26–32] Recent modeling of aggregate lineshapes in oligothiophene thin films,[33,34] oligophenylenevinylene nanocrystals,[35] and polyacene samples[36] has achieved good agreement with experimentally measured lineshapes.

In this paper, we revisit the spectroscopy of the singlet exciton in solid anthracene. We use a strategy similar to that employed in previous studies of tetracene and distyrylbenzene (DSB) aggregate systems.[36–38] To avoid experimental complications such as self-absorption and polariton effects, we study ultrathin polycrystalline films deposited on transparent substrates. To take the role of trap and defect states into account, we time resolve the emission in order to separate the contribution of the initially excited excitons from that of later-appearing trap states. Theoretically, we analyze the temperature-dependent lineshapes in terms of our previously developed model for herringbone polyacene crystals.[31,36] The results of experiment and theory are quantitatively compared at different temperatures. By assuming that the early-time emission originates from a line defect, of a type known to be common in anthracene crystals, we obtain good agreement between experiment and theory for the temperature dependent fluorescence spectral shape. The results indicate that the emissive exciton in our polycrystalline films is delocalized over about ten molecules and, like tetracene,[36] exhibits superradiance at low temperatures. In our samples, the measured decay of the emissive exciton appears to be determined not solely by the radiative decay, but by a trapping process that also becomes more rapid as the temperature is lowered. This more rapid decay is consistent with accelerated trapping due to an increased delocalization of the exciton at lower temperatures. These observations suggest that exciton coherence can play an important role in both radiative and nonradiative decay channels in these materials.

EXPERIMENTAL

The anthracene thin films were made by evaporating ~1 mg of zone refined anthracene (Aldrich, purity ⩾99%) onto a clean glass (or fused quartz) substrate using a vacuum evaporator (Ted Pella Inc., PAC-1) under a vacuum of 3×10^{-5} Torr. The thin films were composed of microcrystalline aggregate domains ranging in size from 200 nm to 2 μm. In order to avoid self-absorption effects, the amount of anthracene evaporated was controlled to limit the height of the anthracene microcrystalline particles to ~100 nm, which results in peak absorption values of ~0.1. The raw absorption spectrum of the thin films is complicated by light scattering from the microcrystalline particles that compose the film, and the actual peak absorption decreases by at least one order of magnitude when the scattering background is subtracted. The thin films were also characterized by atomic force microscopy (AFM) using a Novascan ESPM II in tapping mode to confirm the size of the anthracene microcrystals.

Anthracene single crystals were also grown using vapor sublimation. ~10 mg of zone refined anthracene was placed

in a pyrex tube ~2 in. in height and ~1 in. in diameter. Argon was passed through the tube to remove oxygen. The tube was then sealed and placed in a dark room. The bottom 0.5 in. of the tube was immersed in a silicone oil bath at ~110 °C for the crystals to develop and grow on the cooler top part of the tube. Single crystals ~2 mm in width and >100 μm thick were produced after several days.

Both the microcrystalline thin film and single crystal samples were immediately transferred to a Janis ST-100 continuous flow liquid He cryostat and placed under an inert medium of argon at atmospheric pressure to avoid photo-oxidative damage. The atmospheric pressure of argon is also needed to avoid the rapid sublimation of anthracene crystals which occurs under vacuum at room temperature. The samples were characterized by steady state absorption measurements using an Ocean Optics S-2000 UV-VIS spectrometer and by steady state fluorescence and fluorescence excitation measurements using the Spex Fluorolog Tau-3 fluorescence spectrophotometer. The experiments at room temperature were performed under atmospheric pressure of argon while experiments at low temperatures were performed under an active vacuum of $10^{-4}-10^{-5}$ Torr.

The time resolved fluorescence measurements used femtosecond pulses from a Ti:sapphire oscillator operating at the repetition rate of 91 MHz whose output was tuned to 750 nm. To study fluorescence dynamics at times longer than 10 ns after the laser excitation, the repetition rate of the laser was reduced to 900 kHz using a pulse picker based on a Pockels Cell (Conoptics, 350-160). After reducing the repetition rate to 900 kHz, the 750 nm pulses were compressed with a prism pair and frequency doubled in a 0.4 mm beta barium borate crystal.[37] The resulting 375 nm pulses were filtered using a dichroic mirror and delivered to the cryostat for sample excitation. The fluence of the laser on the sample was ~4 mW/cm^2 and varying the power by a factor of 10 did not change the observed dynamics. For detection, a Hamamatsu C4334 streak camera was used. The streak camera provided both time and wavelength-resolved emission data, with resolutions of 15 ps and 2.5 nm, respectively.

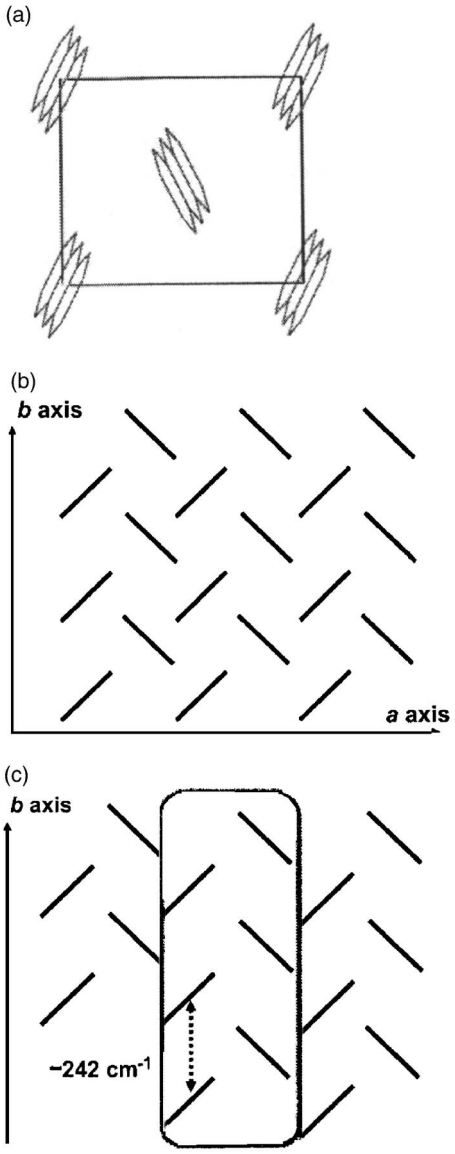

FIG. 1. (a) Top view of the unit cell of the anthracene crystal along the *c* axis. Note the transition dipole moment for the lowest energy excitation lies in the *ab* plane, along the short axis of the molecule. (b) Top view of a two-dimensional aggregate corresponding to the intrinsic crystal structure of anthracene. (c) Top view of a simplified model of a (001)[100] edge dislocation, where the exciton is confined to a linear array of unit cells along the *b* axis. Nearest neighbor molecules within the defect experience a coupling of approximately −242 cm^{-1}, assuming the molecular orientations remain the same as those in the defect-free in the crystal.

THEORETICAL

The crystal unit cell of anthracene is shown in Fig. 1(a). The transition dipole moment of anthracene is oriented along the short molecular axis. The herringbone (HB) packing of the molecules then results in an arrangement of dipoles oriented at an angle of about 60° with respect to their nearest neighbors, as shown in Fig. 1(b). Interactions between closely packed molecules lead to intermolecular exciton states with spectral lineshapes, oscillator strengths, and dynamics significantly different from those of monomeric anthracene. The theoretical framework used to describe such states and their spectroscopic properties is outlined below.

To properly account for the coupling of the first singlet transition in anthracene with the prominent ring-breathing mode at approximately 1400 cm^{-1}, we employ the Holstein-like Hamiltonian[28,39]

$$H = \omega_{0-0} + D + \sum_{\boldsymbol{m}\alpha,\boldsymbol{n}\beta} J_{\boldsymbol{m}\alpha\boldsymbol{n}\beta}|\boldsymbol{m}\alpha\rangle\langle\boldsymbol{n}\beta| + \omega_0\sum_{\boldsymbol{n}\alpha} b^{\dagger}_{\boldsymbol{n}\alpha}b_{\boldsymbol{n}\alpha} + \omega_0\lambda\sum_{\boldsymbol{n}\alpha}(b^{\dagger}_{\boldsymbol{n}\alpha}+b_{\boldsymbol{n}\alpha})|\boldsymbol{n}\alpha\rangle\langle\boldsymbol{n}\alpha| + \lambda^2\omega_0, \quad (1)$$

with $\hbar$ set to unity. The first summation term accounts for resonant energy transfer. The state, $|\boldsymbol{m}\alpha\rangle$, represents a pure electronic state in which the molecule at $\boldsymbol{m}\alpha$ is excited to the first $(1B_u)$ singlet state while all other molecules remain in their electronic ground states. The vector indices $\boldsymbol{m}$ and $\boldsymbol{n}$ identify the unit cells and α,β (=1,2) the two translationally inequivalent molecules within a unit cell. In the gas phase the $1A_g \rightarrow 1B_u$ transition frequency in anthracene is $\omega_{0\text{-}0}$

$\approx 26\,000\ \mathrm{cm}^{-1}$ which shifts to the red by $|D|$ in the crystal due to nonresonant intermolecular interactions. The remaining terms in the Hamiltonian represent the vibrational energy contributions from the symmetric ring-breathing mode with frequency $\omega_0 = 1400\ \mathrm{cm}^{-1}$, with $b^{\dagger}_{\boldsymbol{n}\alpha}(b_{\boldsymbol{n}\alpha})$ the creation (destruction) operator for such a vibration on molecule $\boldsymbol{n}\alpha$. The third summation term accounts for the shift in the nuclear potential well minimum by λ when the molecule is electronically excited, a form of linear exciton-phonon coupling. It is possible to obtain λ from *ab initio* calculations, but it can more reliably be obtained from modeling the experimental fluorescence lineshape. In practice, even a calculated λ would have to be scaled to match the experiment. In our work, the Huang-Rhys factor is set to $\lambda^2 = 1.1$ in order to reproduce relative peak intensities found in the monomer emission spectrum.[40]

In evaluating the electronic (excitonic) interactions $J_{\boldsymbol{m}\alpha\boldsymbol{n}\beta}$ between anthracene molecules $\boldsymbol{m}\alpha$ and $\boldsymbol{n}\beta$, the molecular transition charge densities corresponding to excitation along the short axis of anthracene were calculated quantum mechanically using the semiempirical INDO (Ref. 41) method coupled with a CCSD (Ref. 42) electron correlation scheme. The INDO/CCSD excitation energy of the monomer was computed using a B3LYP/TZVP optimized geometry (TURBOMOLE V5.8).[43] Molecular transition densities were expanded as atom-centered monopoles, and the electronic coupling was calculated as the atom-atom Coulombic sums between interacting molecules within the crystal. The calculated transition dipole moment of $\mu = 2.38$ D is a slight underestimation of the measured moment [$\mu_{\mathrm{exp}} = 2.93$ D (Ref. 44)]; therefore, all interactions were scaled by $(\mu_{\mathrm{exp}}/\mu)^2 = 1.5$. The resulting interactions are nearly identical to those derived by Schlosser and Philpott.[45] Consistent with their findings, all interactions are well-approximated by point dipolar interactions with the exception of the interaction between the two molecules within a single unit cell. A more detailed discussion of all the couplings in the crystal lattice will be deferred to a later paper.[46] For the purposes of this paper, the most relevant coupling is between nearest neighbor molecules along the b axis, which is $-242\ \mathrm{cm}^{-1}$ as shown in Fig. 1(c).

In evaluating aggregate eigenstates and energies we represent the Hamiltonian (1) in a basis set consisting of one- and two-particle states.[39,47,48] The jth such eigenstate with energy ω_j is

$$|\psi^{(j)}\rangle = \sum_{\boldsymbol{n}\alpha}\sum_{\tilde{v}} c^{(j)}_{\boldsymbol{n}\alpha,\tilde{v}}|\boldsymbol{n}\alpha,\tilde{v}\rangle + \sum_{\boldsymbol{n}\alpha,\boldsymbol{m}\beta}\sum_{\tilde{v},v'} c^{(j)}_{\boldsymbol{n}\alpha,\tilde{v};\boldsymbol{m}\beta,v'} \times |\boldsymbol{n}\alpha,\tilde{v};\boldsymbol{m}\beta,v'\rangle. \tag{2}$$

Here $|\boldsymbol{n}\alpha,\tilde{v}\rangle$ is a single-particle vibronic state where the molecule at $\boldsymbol{n}\alpha$ is electronically excited with $\tilde{v}(=0,1,2,\ldots)$ vibrational quanta in the (shifted) excited state nuclear potential. The vibronic/vibrational pair state (two-particle state) $|\boldsymbol{n}\alpha,\tilde{v};\boldsymbol{m}\beta,v'\rangle$ consists of a vibronic excitation at $\boldsymbol{n}\alpha$ and a pure vibrational excitation at $\boldsymbol{m}\beta$ with v' $(=1,2,\ldots)$ quanta in the ground state (unshifted) nuclear potential.

As the first singlet in anthracene lies within the weak electronic coupling [alias strong exciton-phonon (EP) coupling] regime, the absorption is well approximated by transitions to vibronic bands characterized by a given number of excited state vibrational quanta. Furthermore, since the vibronic excitons with the largest oscillator strengths within a given band are primarily delocalized single-particle states we need only retain the single-particle components of the wave function (2) in describing absorption. (Such an approximation is not appropriate for emission, where sideband intensities depend also on two-particle contributions.[30,39]) Assuming periodic boundary conditions, there are two vibronic states in each band—the so called Davydov components—which carry oscillator strength. Optical selection rules dictate that they have wave vector $\boldsymbol{k} = 0$. The two states derive from symmetric (+) and antisymmetric (−) combinations of excitations on the two molecules within the unit cell and can therefore be expanded in symmetrized vibronic excitations

$$|\Psi^{\pm}(\boldsymbol{k}=0,\tilde{v})\rangle = \frac{1}{\sqrt{2N_{\mathrm{cell}}}}\sum_{\boldsymbol{n}}(|\boldsymbol{n}1,\tilde{v}\rangle \pm |\boldsymbol{n}2,\tilde{v}\rangle). \tag{3}$$

The + (−) combination is symmetric (antisymmetric) with respect to a twofold screw rotation along the b direction and therefore has $a_u(b_u)$ character. Moreover, a_u states are polarized along the b axis, while b_u states are polarized perpendicular to the b axis. Due to interband interactions like-symmetry states in Eq. (3) are mixed. To evaluate the mixing coefficients and eigenenergies, the Hamiltonian (1) is represented in the basis set (3) and diagonalized. Our approach reproduces the salient features of the electronic states in crystalline anthracene. The energetic separation between the two Davydov components in the $\tilde{v}=0$ band converges to approximately $185\ \mathrm{cm}^{-1}$ in a 100×100 cell aggregate. (As shown by Schlosser and Philpott, interactions between dipoles in differing HB planes do not significantly contribute to the dipole sum for excitation normal to the HB plane.[45]) Our calculated Davydov splitting is in good agreement with experimental measurements of $190\ \mathrm{cm}^{-1}$ (Ref. 49) and $210\ \mathrm{cm}^{-1}$ (Ref. 50) for excitation normal to the ab plane. Moreover, the lower (upper) Davydov components are b-(ac) polarized with the b/ac polarization ratio of about 5, also in good agreement with the measured value.[49,50]

The β-polarized emission spectrum $S_{\beta}(\omega;T)$ at temperature T is evaluated by averaging over emission from all thermally excited states. With the jth state having transition frequency ω_j, the emission spectrum becomes

$$S_{\beta}(\omega;T) = \omega_{\mathrm{em}}^{-3}\sum_{v_t=0,1,2,\ldots}\langle I^{0-v_t}_{j;\beta}(\omega_j - v_t\omega_0)^3 \times W_e(\omega-\omega_j+v_t\omega_0)\rangle_T, \tag{4}$$

where $\beta = a', b, c$ (with $a' \perp b, c$) and ω_{em} is the emission frequency for the lowest energy state ($j=1$). The thermal average in Eq. (4) is denoted by $\langle\cdots\rangle_T$. For a j-dependent quantity, say, g_j, the thermal average is given by

$$\langle g_j\rangle_T = \frac{1}{Z(T)}\sum_j g_j e^{-\hbar(\omega_j-\omega_{em})/kT}, \tag{5}$$

with the partition function defined as, $Z(T) \equiv \Sigma_j \exp[-\hbar(\omega_j-\omega_{em})/kT]$. In Eq. (4), $I^{0-v_t}_{j;\beta}$ is the (dimensionless) β-polarized transition strength for all photons originat-

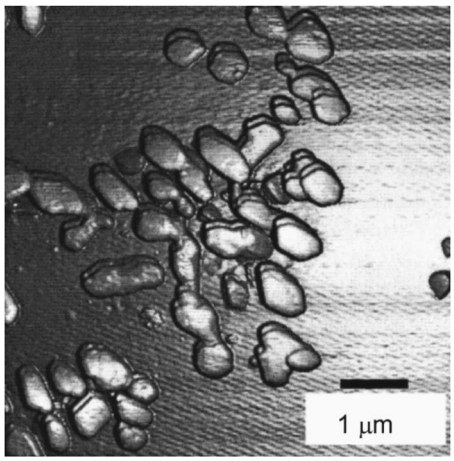

FIG. 2. AFM image of a thin evaporated film with submicron islands distributed over the substrate.

ing from the jth excited state and terminating on the ground electronic state with v_t total vibrational quanta

$$I_{j;\beta}^{0-v_t} = \frac{1}{\mu^2} \sum_{\{v_n\}}{}' |\langle \psi^{(j)} | \hat{\mu}_\beta \prod_n |g_n, v_n\rangle|^2. \quad (6)$$

In Eq. (6) $\hat{\mu}_\beta$ is the β component of the aggregate transition dipole moment operator. The sum is over all terminal states, $\Pi_n |g_n, v_n\rangle$, where all molecules are in their electronic ground states but with a distribution $\{v_n\}$ of vibrational excitations. The prime on the summation indicates that the vibrational distribution is constrained so that the total number of quanta is $v_t \equiv \Sigma_n v_n$. We note that the vibrational quanta pertain to the ground (unshifted) nuclear potential. The jth thermally excited state therefore contributes a vibronic progression with peak frequencies at $\omega_j - v_t \omega_0$. Finally, $W_e(\omega)$ in Eq. (4) is a Gaussian lineshape function with a width adjusted to reproduce the experimental spectral broadening. Note that Eq. (4) does not account for temperature-dependent homogeneous line broadening, as may occur through enhanced exciton-lattice phonon scattering, for example.

RESULTS AND DISCUSSION

In order to make ultrathin films of anthracene, we relied on vacuum evaporation onto cleaned glass substrates. This process does not lead to uniform films but instead results in submicron islands that are uniformly distributed over the substrate. An AFM image of a film used in our spectroscopy experiments is shown in Fig. 2. The presence of the islands leads to a wavelength-dependent scattering background in a standard absorption measurement. Absorption measurements confirmed that the peak optical absorbance of our samples was less than 0.1 even before removal of the scattering background. Fluorescence excitation spectra are less sensitive to scattering and thus provide a better representation of the true absorption spectrum of the anthracene aggregates. The excitation spectrum is shown in Fig. 3 for both room temperature and 80 K. Other than a slight sharpening of the vibronic peaks at 80 K, the two spectra are identical. Note that unlike tetracene, there is no clear Davydov splitting in the anthracene absorption. The Davydov splitting in anthracene is estimated to be ~ 200 cm^{-1},[49–52] as opposed to >600 cm^{-1} for tetracene,[7] and this small splitting is swamped by the broadening of the spectrum due to both homogeneous and inhomogeneous contributions to the linewidth. Finally, the low coverage of anthracene, with islands on the order of the wavelength of light or smaller, prevents the formation of polaritons in these samples, which would complicate the interpretation of the optical spectra.[53–55]

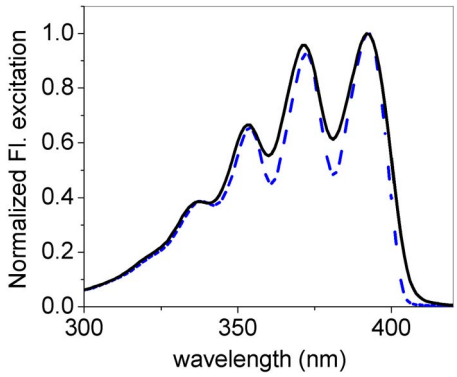

FIG. 3. (Color online) Steady state fluorescence excitation spectra (λ_{em} =440 nm) of an anthracene microcrystalline thin film at 296 K (solid line) and 80 K (long dash line).

While the absorption lineshape is largely temperature independent, the steady state fluorescence spectrum changes significantly as the temperature is lowered. Previous work has shown how the temperature dependence of the fluorescence can provide valuable information about the Frenkel exciton delocalization in organic solids.[35,36] But in order to ensure that the measured spectra accurately reflect the intrinsic molecular species in solid anthracene, we must address the issue of self-absorption, which is known to distort both the spectral shape and decay of anthracene luminescence.[56–58] Figure 4 shows the measured room temperature fluorescence spectra for three different samples: a single crystal that is ~ 0.5 mm thick, an evaporated film that is <1 μm thick with a maximum absorbance of 2.0, and an ultrathin film that is less than 0.1 μm thick with a maximum absorbance of <0.04. The ultrathin film thickness is chosen to be sufficiently thin that even sparser films, with lower

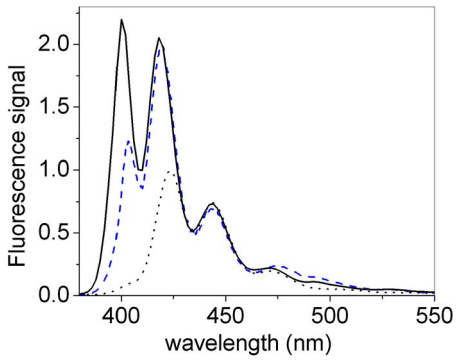

FIG. 4. (Color online) Normalized room temperature (296 K) steady state fluorescence spectra of an anthracene single crystal (short dash line), the fluorescence of a thick evaporated film with a maximum outside diameter (O.D.)~ 2 (long dash line) and the emission of a thin film with maximum O.D.<0.04 (solid line). All spectra have been normalized to match the single crystal spectrum at 440 nm.

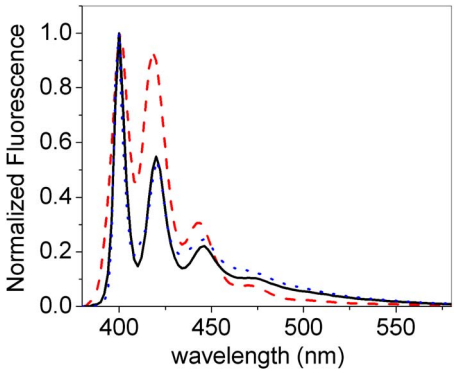

FIG. 5. (Color online) The normalized steady state fluorescence spectra (λ_{exc}=360 nm) of anthracene microcrystalline thin films at 296 K (long dash line), 80 K (short dash line), and 10 K (solid line).

absorption values, still give the same fluorescence lineshape. All three spectra exhibit the expected vibronic progression, and all three have variously been reported in the literature as the luminescence spectrum of solid anthracene.[56] In most measurements, the high energy side of the luminescence is strongly attenuated by self-absorption, and the true shape of the vibronic spectrum is obscured. We found experimentally that only at peak absorbances of 0.1 and lower did the spectral shape of the fluorescence cease to depend on film thickness. Spectra similar to our ultrathin film spectrum have been reported for anthracene microcrystals immersed in a high refractive index fluid,[59] and for microcrystalline film spectra which have been carefully corrected for reabsorption.[56] In Fig. 5, we show the normalized steady state fluorescence data from an ultrathin sample at 296, 80, and also 10 K, which can be compared with the excitation data in Fig. 3. The high energy peak, no longer attenuated by self-absorption, grows by 70% in height, while the low energy wing is diminished. The dramatic shape change in the emission is in stark contrast to the negligible change in the absorption spectrum.

The problem with analyzing the steady state luminescence by itself is that it usually contains contributions from multiple types of species. In previous work on molecular crystal systems,[36,37] we observed nonexponential fluorescence decays, with spectra that changed depending on the detection window. This is also observed in our anthracene films. In a separate series of experiments, using streak camera detection in conjunction with a liquid helium cryostat, we have measured the time- and wavelength-resolved luminescence of anthracene films at temperatures ranging from 10 to 295 K. At all temperatures, the emission lineshape changes over the course of nanoseconds. In Fig. 6, we show this behavior for three temperatures: 10, 80, and 295 K. At all three temperatures, the initial 0–200 ps spectrum is a blueshifted vibronic progression with a dominant peak at 398 nm. In the 7–9 ns window, the 295 K spectrum is largely unchanged, while the lower temperature 7–9 ns spectra are clearly redshifted and have different shapes. In order to analyze this data, and to resolve the individual component spectra, we require a model for the excited state that takes into account contributions from at least two different electronic species.

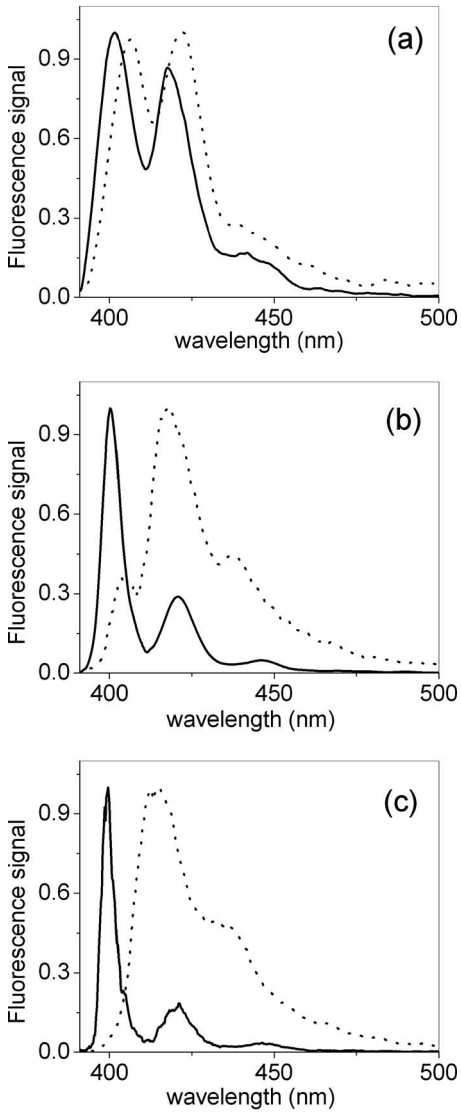

FIG. 6. Normalized fluorescence spectra at (a) 296 K, (b) 80 K, and (c) 10 K for time delays of 0–200 ps after laser excitation (solid line) and 7–9 ns after laser excitation (short dash line).

For the data at lower temperatures, we use an approach developed previously to analyze experiments in DSB.[37] The simplest possible model to describe the fluorescence decay dynamics is outlined in Fig. 7. State 1 corresponds to the

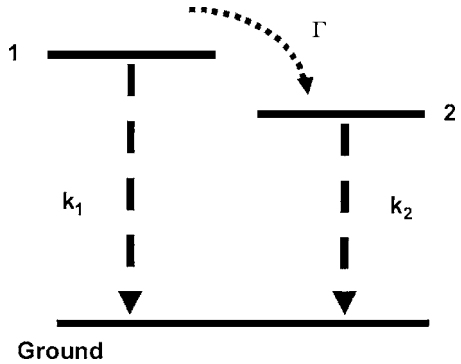

FIG. 7. Energy level diagram for analysis of the experimental data. Level 1 corresponds to the intrinsic exciton, whereas level 2 represents lower energy defect states.

exciton that emits at early times, while state 2 corresponds to a lower energy trap state whose emission grows in at later times. The states decay to the ground state with rates k_1 and k_2, and population can also be transferred (irreversibly) from state 1 to state 2 with rate Γ. This model leads to the two coupled differential equations

$$\frac{dN_1}{dt} = -(k_1 + \Gamma)N_1, \tag{7}$$

$$\frac{dN_2}{dt} = \Gamma N_1 - k_2 N_2. \tag{8}$$

To model the time-dependent emission spectrum we define the emission spectra of levels 1 and 2 to be $F_1(\lambda)$ and $F_2(\lambda)$, respectively. The measured fluorescence signal $F_{\text{tot}}(\lambda,t)$ will be the sum of the contributions from levels 1 and 2,

$$F_{\text{tot}}(\lambda,t) = N_1(t)F_1(\lambda) + N_2(t)F_2(\lambda) \tag{9}$$

or more explicitly,

$$F_{\text{tot}}(\lambda,t) = N_1^0 e^{-(k_1+\Gamma)t}F_1(\lambda) + \left[-\frac{N_1^0\Gamma}{(k_1+\Gamma)-k_2}e^{-(k_1+\Gamma)t} + \left(N_2^0 + \frac{N_1^0\Gamma}{(k_1+\Gamma)-k_2}\right)e^{-k_2 t}\right]F_2(\lambda), \tag{10}$$

where $N_1^0 = N_1(t=0)$ and $N_2^0 = N_2(t=0)$. When $t=0$,

$$F_{\text{tot}}(\lambda, t=0) = N_1^0 F_1(\lambda) + N_2^0 F_2(\lambda). \tag{11}$$

In order to fit the data, we begin by assuming $N_2^0 = 0$, which makes Eq. (11) $F_{\text{tot}}(\lambda, t=0) = N_1^0 F_1(\lambda)$. In this case, every exciton is initially in state 1 and no population exists in 2. Thus we take the initial spectrum as $F_1(\lambda)$, the spectrum of state 1 and the longer time spectrum as $F_2(\lambda)$. Experimentally, $F_1(\lambda)$ is taken from the spectrum integrated in the 0–200 ps time window. $F_2(\lambda)$ is taken from the spectrum integrated in the 5–9 ns time window. Ideally, we would now be able to fit the data at all times and wavelengths by varying the kinetic parameters k_1, Γ, and k_2. Unfortunately, we found that we needed a value of $N_2^0 \neq 0$ in order to reproduce the data. Typically, $N_2^0 \leqslant 0.12 N_1^0$ at all temperatures. In principle we should iteratively vary the parameters N_2^0, k_1, Γ, and k_2 to generate new $F_1(\lambda)$ and $F_2(\lambda)$ profiles. In practice, it is doubtful that the simplistic three-state model in Fig. 7 justifies this type of extensive effort, and such refinements would only result in at most 10% changes in the spectral amplitudes.

Taking the measured short (0–200 ps) and long (5–9 ns) emission spectra to represent those of states 1 and 2, respectively, we can perform a global fit of our fluorescence decay data. In this fit, k_1, Γ, k_2, and N_2^0, the relative amount of population directly excited into state 2, are variable parameters. Using this simple model for the excited state dynamics, we can reproduce the observed time- and wavelength-resolved dynamics of the anthracene emission reasonably well. Table I gives the kinetic parameters obtained in this way. An example of how our model fits the data is given in Fig. 8, where the time-dependent signals at two different wavelengths, 400 and 600 nm, are compared to the signals calculated using the model parameters summarized in Table I. Both the rapid decay of the blue component and the growth and slower decay of the red component are reasonably well described by the model.

TABLE I. Kinetic values for the model in Fig. 7 obtained from modeling the experimental fluorescence decays. na= not applicable; only a single decay component could be resolved at 295 K.

Temperature (K)	$k_1+\Gamma$ (ns^{-1})	k_2 (ns^{-1})	Γ (ns^{-1})
10	1.26 ± 0.17	0.23 ± 0.03	0.87 ± 0.15
25	1.19 ± 0.15	0.21 ± 0.03	0.70 ± 0.14
80	0.96 ± 0.07	0.20 ± 0.03	0.43 ± 0.09
150	0.72 ± 0.05	0.21 ± 0.03	0.43 ± 0.07
295	0.25 ± 0.04	na	na

In Fig. 9, we plot the temperature dependence of the parameters in our model. The total decay rate of state 1, described by $k_1+\Gamma$, is strongly temperature dependent, and in a nonintuitive way—the decay becomes more rapid as the temperature decreases. Figure 9(a) shows that $k_1+\Gamma$ increases by a factor of ~5 in going from 295 to 10 K. A similar temperature dependence of fluorescence decay rate has been observed previously for crystalline anthracene samples, although the absolute value of the decay time varies significantly.[60–62] Table I gives both the $k_1+\Gamma$ and Γ fit parameters, with most of the uncertainty coming from Γ, which is obtained by analyzing the growth of the noisier low energy part of the spectrum shown in Fig. 8. Nevertheless, it is clear that both rates increase with decreasing temperature. k_2 and the relative weighting of N_2^0, plotted in Figs. 9(b) and 9(c), show almost no temperature dependence over the same range. Our data show that while the spectrum and decay of state 1 undergo dramatic changes with temperature, only the spectral shape of the lower energy state 2 is temperature dependent, while its lifetime and excitation probability do not change appreciably.

The next question concerns the identity of states 1 and 2. The simplest assumption would be that state 1 arises from a two-dimensional (2D) aggregate like the one pictured in Fig. 1(b), which is intrinsic to the ideal structure of the anthracene crystal. It is well known, however, that crystal defects

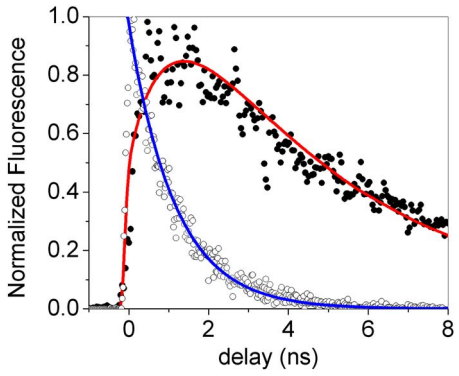

FIG. 8. (Color online) Time evolution of the normalized emission from state 1 measured at 400 nm (○) and state 2 measured at 600 nm (●) at 80 K. The red and green lines are the fits to the 1 and 2 emissions, respectively, using the decay rate constants k_1, Γ, and k_2, and an adjustable parameter N_2^0, which is the initial population in state 2 created by the excitation pulse.

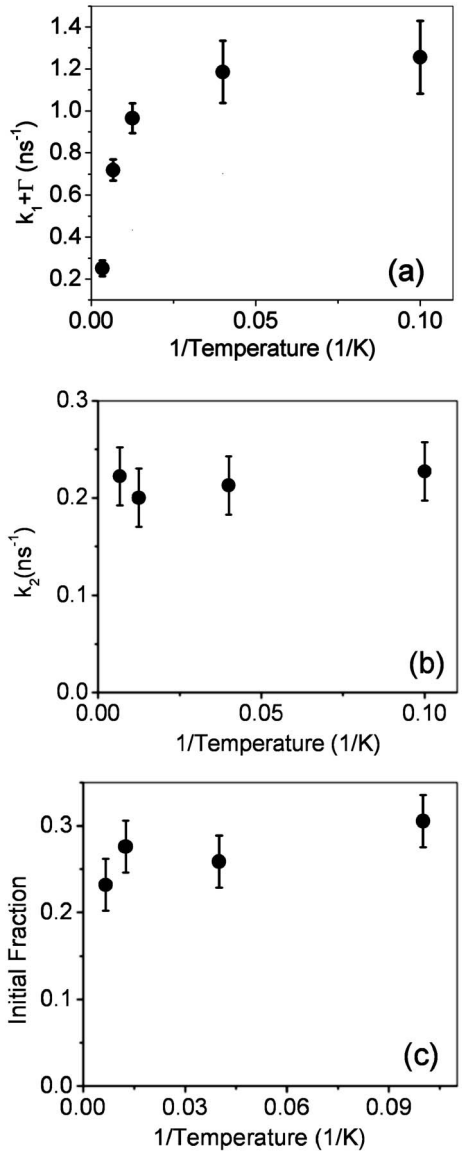

FIG. 9. (a) Temperature dependence of the decay rate of state 1 and the growth rate of state 2 (trap). (b) Temperature dependence of the decay rate of state 2. (c) $N_2^0/(N_1^0\Gamma/[(k_1+\Gamma)-k_2])$, the relative ratio of the initial population in state 2 created by the excitation pulse to that created by trapping of excitons from state 1.

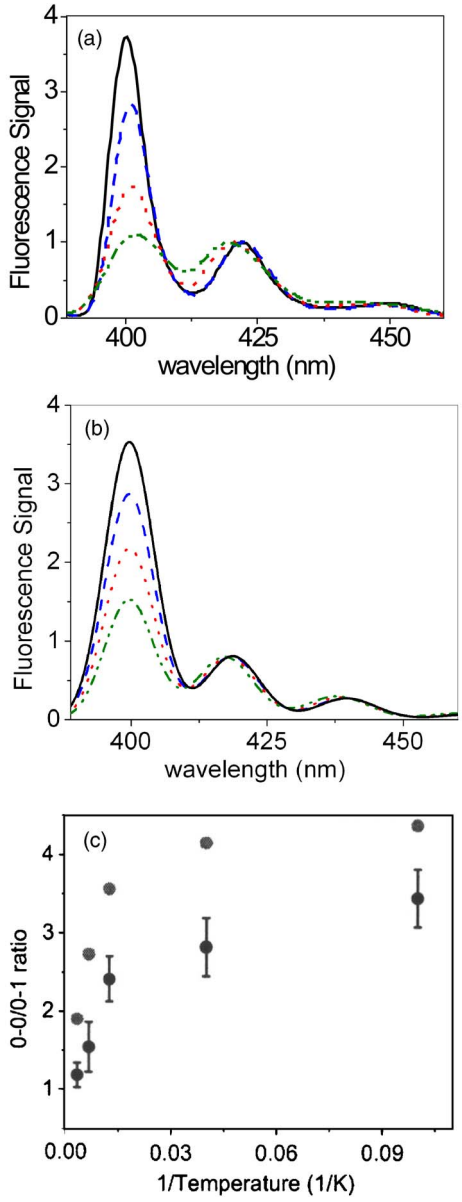

FIG. 10. (Color online) (a) Experimental and (b) calculated spectra using a 1×4 array of anthracene unit cells as described in the Theoretical section at 296 K (dash-dot-dot line), 150 K (short dash line), 80 K (long dash line), and 10 K (solid line). (c) The temperature dependence of the ratio of the 0-0 to 0-1 peak areas for the data (●) and the theoretical model (○).

can play an important role in both the absorption[63] and luminescence of anthracene single crystals.[64–72] The literature contains many examples of shallow dislocation defects as well as deeper stacking faults.[73] Evaporated polycrystalline films are likely to contain a high concentration of such defects.[74] Our suspicion that defects play a decisive role in the observed emission is heightened by the fact that the linewidths in our emission spectra are on the order of 200 cm^{-1} even at 10 K. This linewidth is a factor of 5 greater than what has been observed for single crystal fluorescence,[64,66] although in those samples self-absorption prevented a quantitative analysis of the relative intensities of the vibronic lines, as done in this paper. The increased vibronic linewidth in anthracene crystals has been attributed to coupling to defects.[75] In addition, after extensive theoretical analysis, which will be detailed in a subsequent paper,[46] it became clear that the 2D aggregate could not give rise to the observed temperature dependence of the spectrum. In order to describe the emission we have to consider the existence of structural defects, which serve to dimensionally confine the exciton. Here we focus on one-dimensional aggregates broadly representative of edge dislocations ("line" defects).[76] For one-dimensional (1D) defects we consider a linear array of unit cells along *b*, which is a simplified model for the common (001) [100] edge dislocation which is shown in Fig. 1(c). Figures 10(a) and 10(b) compares our experimentally obtained spectra for state 1 at different temperatures with spectra calculated using a 1×4 array of anthracene unit cells. Note that the experimental spectra have been corrected for variations in laser power and coverage but have not been scaled to match each other. Both the relative areas of the peak and their change with temperature are well described by

the 1×4 domain model. Figure 10(c) compares the temperature dependence of the ratio of the 0-0 to 0-1 peak areas for both the data and the theoretical model, showing reasonable agreement between them, especially after a slight offset in the calculated points is taken into account (see below).

In prior work we have emphasized a fundamental difference between the 0-0 (origin) and sideband emissions (0-1, 0-2,…) in HB aggregates of OPV*n* and OT*n*.[30,31,39,77] Briefly, the former is responsive to the exciton coherence volume while the latter is not. Hence, the 0-0 to 0-1 intensity ratio is a simple measure of the exciton coherence number, once self-absorption, index changes, etc., have been accounted for. The level structure of the *b*-directed defect in Fig. 1(c) can be understood in terms of two weakly interacting subaggregates, where molecules within each subaggregate are translationally equivalent. Such subaggregates are *J* aggregates because of the strong and negative coupling (-242 cm^{-1} for nearest neighbors) placing the optically allowed ($\boldsymbol{k}=0$) state at the exciton band bottom. The two lowest energy states of the combined aggregate are in fact the two Davydov components with the *b*-polarized lower Davydov component possessing roughly 5 times the oscillator strength as the upper (ac-polarized) component. The lowest energy state is denoted as $|em_b\rangle$ with energy ω_{em_b}.

The dependence of the emission spectrum of linear "defect" aggregates on the number of chromophores *N* and temperature *T* is most easily appreciated in the limit of large *N* so that end effects are negligible, or for finite *N* if periodic boundary conditions are invoked. In this case the (dominant) *b*-polarized 0-0 intensity from Eq. (4) simplifies to

$$S_b(\omega=\omega_{em_b};T)=\langle I_b^{0\text{-}0}\rangle_T W_e(\omega-\omega_{em_b}), \tag{12}$$

where the thermally averaged 0-0 line strength is

$$\langle I_b^{0\text{-}0}\rangle_T=|\langle\psi^{(em_b)}|\hat{\mu}_b|G\rangle|^2/Z(T)\mu^2. \tag{13}$$

Inserting the wave function from Eq. (2) into Eq. (13) results in a simple form for the *b*-polarized 0-0 line strength[30,39]

$$\langle I_b^{0\text{-}0}\rangle_T=Z(T)^{-1}NF(\mu_b/\mu^2), \tag{14}$$

where *F* is a generalized Franck-Condon factor ranging from $\exp(-\lambda^2)$ in the strong EP coupling limit to unity in the weak EP coupling limit, and μ_b is the component of the molecular dipole moment along the *b* axis (for anthracene our calculations predict $|\mu_b/\mu|=0.90$). Equation (14) shows that the line strength of the 0-0 transition is coherently enhanced by a factor of *N* at low temperatures such that the partition function remains near unity. Furthermore, $\langle I_b^{0\text{-}0}\rangle_T$ decreases monotonically with increasing temperature as $Z(T)$ increases. Physically this reflects the fact that thermally excited excitons with nonzero $\boldsymbol{k}$ cannot contribute to 0-0 emission by virtue of the $\Delta\boldsymbol{k}=0$ optical selection rule. In the high temperature limit the dependence of the 0-0 emission strength on *N* is lost, and the factor of N/Z in Eq. (14) is replaced by the thermal coherence size N_T. As shown previously,[31] $I^{0\text{-}0}$ in Eq. (14) reduces to $N_T F(\mu_b/\mu^2)$ in a square HB lattice, where the thermal coherence number is $N_T=1+4\pi\omega_c/kT$ and ω_c is the scaled curvature at the band bottom.

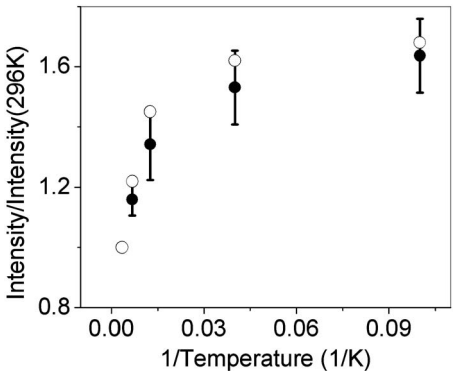

FIG. 11. The integrated fluorescence intensity ratio, taken within the short time window (0–200 ps), as a function of temperature for the data (●) and the theoretical model (○). This quantity should reflect the radiative rate, as outlined in Eq. (17). Note that experimental points at room temperature are both 1.0, so only the theoretical point is shown.

By contrast, the replica line strengths ($I^{0\text{-}1}, I^{0\text{-}2},\ldots$) are insensitive to the exciton coherence size *N*, as well as temperature, as was shown in detail for DSB and OT*n* aggregates.[30,31,39] The sideband transitions are not limited by the $\Delta\boldsymbol{k}=0$ selection rule since termination on any number of ground state phonons can satisfy momentum conservation. Hence, in contrast to the 0-0 peak, sideband intensities are practically independent of temperature, with the exception of a small blueshift due to emission from thermally excited states.

The temperature dependence discussed in the preceding paragraphs is seen clearly in both the measured early-time spectra in Fig. 10(a) as well as the calculated spectra in Fig. 10(b). based on an aggregate with $N=8$ molecules. Although not shown, larger aggregates differ only in an enhanced 0-0 peak at lower temperatures, reflecting an increased coherence number *N*. The value of *N* which best captures the enhanced 0-0 peak intensity at low temperature is approximately 10. At the highest temperature, the calculated 0-0 intensity, although practically independent of *N*, remains almost twice as intense as the first sideband in contrast to experiment, where the ratio is closer to 1. This is what gives rise to the offset seen for the calculated points in Fig. 10(c). We believe the discrepancy is due to additional disorder within the linear aggregates not accounted for in the model. Such disorder also serves to define a coherence number N_{coh} which is likely to be much smaller than the actual number of molecules (*N*) in the defect. We expect the relation (14) to approximately hold with *N* replaced by N_{coh}, where N_{coh} is approximately 10.

The trend in relative quantum yield of the state 1 fluorescence is also well reproduced by calculations based on the 1×4 aggregate. Figure 11 shows the relative yield of fluorescence, taken as being proportional to the integrated fluorescence within the short time window (0–200 ps) as a function of temperature. The general relation between these two quantities can be derived simply. Assuming that state 1, with an initial population $N_{\mathrm{ex}}(0)$, decays through both radiative (k_{rad}) and nonradiative (k_{nr}) mechanisms, we have

$$S(t) \propto k_{\mathrm{rad}} N_{\mathrm{ex}}(0) \exp[-(k_{\mathrm{rad}} + k_{\mathrm{nr}})t], \tag{15}$$

where $S(t)$ is the detected number of photons. If we integrate the signal over a period τ, we find

$$\int_0^{\tau} dt S(t) \propto k_{\mathrm{rad}} N_{\mathrm{ex}}(0) \frac{1 - \exp[-(k_{\mathrm{rad}} + k_{\mathrm{nr}})\tau]}{k_{\mathrm{rad}} + k_{\mathrm{nr}}}. \tag{16}$$

If τ is very short, such that $(k_{\mathrm{rad}}+k_{\mathrm{nr}})\tau \ll 1$, then we have

$$\int_0^{\tau} dt S(t) \propto k_{\mathrm{rad}} N_{\mathrm{ex}}(0) \tau. \tag{17}$$

Thus the integrated fluorescence intensity at very short times depends only on k_{rad}, assuming that $N_{\mathrm{ex}}(0)$ and τ remain constant with temperature. We chose $\tau = 200$ ps. The integrated fluorescence signals and those from the 1×4 calculations are scaled to unity at T=295 K and plotted in Fig. 11. In both cases, the increase in the early time fluorescence, which parallels k_{rad}, is due to the increased exciton coherence length at lower temperatures and is commonly referred to as superradiance. As in our earlier work on tetracene,[36] the theoretical model quantitatively predicts the temperature dependent behavior of two independent observables: the spectral shape and the radiative rate.

Although the theoretical model does a good job of predicting the observed trend in the early-time quantum yield, it also raises some questions about the absolute magnitudes of the experimental decay rates. In the simplest picture, $k_1 = k_{\mathrm{rad}}$ and Γ is a trapping rate that likely depends on sample morphology and trap density. The radiative lifetime of monomeric anthracene is 18–20 ns,[78] which leads to a monomer radiative decay rate $k_{\mathrm{rad}}^{\mathrm{monomer}} \cong 0.05\ \mathrm{ns}^{-1}$. Given the 1×4 aggregate model, the radiative rate at the lowest temperatures should be enhanced by almost a factor of 3, with the calculated $k_{\mathrm{rad}} = 0.14\ \mathrm{ns}^{-1}$. At low temperatures, the decay rate k_1 extracted from the values in Table I ranges from 0.40 to 0.50 ns^{-1} and is larger than the theoretically predicted k_{rad} value. It is possible that even after explicitly taking the trapping to state 2 into account via Γ, k_1 still contains contributions from other nonradiative processes. Two obvious candidates are internal conversion and intersystem crossing, but both types of processes are expected to be thermally activated, with rates decreasing with temperature. k_1 appears to have the opposite temperature dependence: it increases from about 0.30 ns^{-1} at 295 K to 0.40–0.50 ns^{-1} at low temperatures, and this change is close to the error in the measured decay values. Another possibility is that the trapping process is not completely described by Γ, which only takes into account trapping to bright states. It is likely that there exists an appreciable density of dark trap states as well. A dark state trapping term with a weak temperature dependence provides a way to increase k_1 and retain the superradiant temperature dependence observed experimentally. A final question is why the exciton trapping rate, as manifested in either k_1 or Γ, would exhibit "superradiant" behavior. As originally pointed out by Mobius and Kuhn,[10,79] delocalization at lower temperatures increases the spatial extent of the exciton, which increases its cross section for interacting with the localized trap sites. Ignoring possible complications due to temperature dependent trapping probabilities and diffusion rates, the trapping rate is proportional to the inverse of the coherence length, just like the radiative rate. This provides a qualitative explanation for the observed temperature dependence of $k_1+\Gamma$, since both the radiative and nonradiative rates increase linearly with the exciton coherence length.

The picture that emerges is that emission from anthracene nanoaggregates is most likely due to a one-dimensional structural defect which maintains exciton coherence along the one-dimensional conduit. Good agreement with experiment is obtained for the *b*-directed defect aggregates comprised of approximately ten molecules which correlate to the edge dislocations, (001)[100]. We emphasize that the coherence number is most likely far smaller than the actual number of molecules comprising the defect due to additional sources of disorder—for example, site disorder, which also act to limit the coherence size of the exciton. Also, other types of defects with the same type of intermolecular coupling, i.e., *J*-type aggregates, could give rise to a similar behavior and cannot be excluded from playing a role in the luminescence. A separate question is whether our assumption that only a single intramolecular vibrational mode dominates the spectroscopy is accurate. We have recently shown that low frequency mode progressions can be suppressed by excitonic coupling in oligothiophenes.[34] Since the single mode theory also does a good job describing the spectroscopy experiments in the current paper, similar considerations are expected to apply to anthracene. Perhaps the most interesting question raised by this work is the fate of the intrinsic exciton of defect-free anthracene, which should reside in the 2D aggregates in Fig. 1(b). This state may be very shortlived due to defect trapping, and it may be possible that examination of our films with higher time resolution could capture the decay of an even more blueshifted species that reflects the directly excited 2D exciton state.

CONCLUSION

In this work, we have investigated the electronic states that give rise to the spectroscopic behavior of solid anthracene. To accomplish this, we have used a combination of experimental techniques. In order to avoid the distorting effects of self-absorption, we studied ultrathin evaporated films. In order to isolate the contributions of different emitting states, we used a streak camera to detect the time- and wavelength-resolved fluorescence. The temperature dependent changes observed in the spectrum and quantum yield of the exciton are quantitatively reproduced using a model that assumes the thin film emission is dominated by linear defect aggregates (dislocations) containing approximately ten monomers. Within these domains, the exciton's coherence length steadily increases as the temperature drops, until it reaches the limits of the domain, whereupon it saturates and remains constant as the temperature is lowered further. Our results show that the spectroscopy of polyacene solids can be analyzed to obtain quantitative information about the states that underlie the interesting electronic properties of these materials.

ACKNOWLEDGMENTS

One of the authors (C.J.B.) acknowledges support from the National Science Foundation, Grant No. CHE-0719039. Another author (F.C.S.) is supported by the National Science Foundation, Grant No. DMR-0606028. The work at Georgia Tech has been partly supported by the Office of Naval Research under Grant No. N00014-04-1-0120 and the CRIF Program of the National Science Foundation under Award No. CHE-0443564. This work of another author (D.B.) was supported by the European Commission through the STREP project MODECOM (NMP-CT-2006-016434). The authors gratefully acknowledge the Belgian National Fund for Scientific Research (FNRS-FRFC) for its financial support. One of the authors (D.B.) is a FNRS research associate.

[1] E. A. Silinsh and V. Capek, *Organic Molecular Crystals* (AIP, New York, 1994).
[2] J. D. Wright, *Molecular Crystals*, 2nd ed. (Cambridge University Press, Cambrdige, UK, 1995).
[3] D. Moses, C. Soci, X. Chi, and A. P. Ramirez, Phys. Rev. Lett. **97**, 067401/1 (2006).
[4] H. Marciniak, M. Fiebig, M. Huth, S. Schiefer, B. Nickel, F. Selmaier, and S. Lochbrunner, Phys. Rev. Lett. **99**, 176402/1 (2007).
[5] G. D. Mahan, J. Chem. Phys. **41**, 2930 (1964).
[6] R. Silbey, J. Jortner, and S. A. Rice, J. Chem. Phys. **42**, 1515 (1965).
[7] M. R. Philpott, J. Chem. Phys. **50**, 5117 (1969).
[8] M. Sceats and S. A. Rice, Chem. Phys. Lett. **44**, 425 (1976).
[9] R. M. Hochstrasser, Rev. Mod. Phys. **34**, 531 (1962).
[10] *J-aggregates*, edited by T. Kobayashi (World Scientific, Singapore, 1996).
[11] D. Mobius, Adv. Mater. (Weinheim, Ger.) **7**, 437 (1995).
[12] H. Fidder and D. A. Wiersma, Phys. Status Solidi B **188**, 285 (1995).
[13] T. Pullerits and V. Sundstrom, Acc. Chem. Res. **29**, 381 (1996).
[14] R. Monshouwer, M. Abrahamsson, F. V. Mourik, and R. V. Grondelle, J. Phys. Chem. B **101**, 7241 (1997).
[15] R. Kumble and R. M. Hochstrasser, J. Chem. Phys. **109**, 855 (1998).
[16] L. D. Book, A. E. Ostafin, N. Ponomarenko, J. R. Norris, and N. F. Scherer, J. Phys. Chem. B **104**, 8295 (2000).
[17] M. Dahlbom, T. Pullerits, S. Mukamel, and V. Sundstrom, J. Phys. Chem. B **105**, 5515 (2001).
[18] A. Damjanovic, I. Kosztin, U. Kleinekathofer, and K. Schulten, Phys. Rev. E **65**, 031919/1 (2002).
[19] G. D. Scholes and G. R. Fleming, Adv. Chem. Phys. **132**, 57 (2006).
[20] S. Tavazzi, M. Campione, M. Laicini, L. Raimondo, A. Borghesi, and P. Spearman, J. Chem. Phys. **124**, 194710/1 (2006).
[21] H. Fidder, J. Knoester, and D. A. Wiersma, J. Chem. Phys. **95**, 7880 (1991).
[22] M. V. Burgel, D. A. Wiersma, and K. Duppen, J. Chem. Phys. **102**, 20 (1995).
[23] E. O. Potma and D. A. Wiersma, J. Chem. Phys. **108**, 4894 (1998).
[24] K. Ohta, M. Yang, and G. R. Fleming, J. Chem. Phys. **115**, 7609 (2001).
[25] S. Jang, M. D. Newton, and R. J. Silbey, J. Phys. Chem. B **111**, 6807 (2007).
[26] A. Witkowski and W. Moffitt, J. Chem. Phys. **33**, 872 (1960).
[27] R. L. Fulton and M. Gouterman, J. Chem. Phys. **41**, 2280 (1964).
[28] P. O. J. Scherer and S. F. Fischer, Chem. Phys. **86**, 269 (1984).
[29] F. C. Spano and S. Siddiqui, Chem. Phys. Lett. **314**, 481 (1999).
[30] F. C. Spano, J. Chem. Phys. **118**, 981 (2003).
[31] F. C. Spano, J. Chem. Phys. **120**, 7643 (2004).
[32] F. C. Spano, Annu. Rev. Phys. Chem. **57**, 217 (2006).
[33] J. Clark, C. Silva, R. H. Friend, and F. C. Spano, Phys. Rev. Lett. **98**, 206406/1 (2007).
[34] Z. Zhao and F. C. Spano, J. Phys. Chem. C **126**, 6113 (2007).
[35] F. C. Spano, Phys. Rev. B **71**, 235208/1 (2005).
[36] S. H. Lim, T. G. Bjorklund, F. C. Spano, and C. J. Bardeen, Phys. Rev. Lett. **92**, 107402/1 (2004).
[37] S. H. Lim, T. G. Bjorklund, and C. J. Bardeen, J. Phys. Chem. B **108**, 4289 (2004).
[38] M. Voigt, A. Langner, P. Schouwink, J. M. Lupton, R. F. Mahrt, and M. Sokolowski, J. Chem. Phys. **127**, 114705/1 (2007).
[39] F. C. Spano, J. Chem. Phys. **116**, 5877 (2002).
[40] I. B. Berlman, *Handbook of Fluorescence Spectra of Aromatic Molecules*, 2nd ed. (Academic, New York, 1971).
[41] J. Ridley and M. Zerner, Theor. Chim. Acta **32**, 111 (1973).
[42] S. Hirata, M. Nooijen, and R. J. Bartlett, Chem. Phys. Lett. **326**, 255 (2000).
[43] R. Ahlrichs, M. Baer, M. Haeser, H. Horn, and C. Koelmel, Chem. Phys. Lett. **162**, 165 (1989).
[44] M. R. Philpott, J. Chem. Phys. **59**, 4406 (1973).
[45] D. W. Schlosser and M. R. Philpott, J. Chem. Phys. **77**, 1969 (1982).
[46] J. E. Norton, T. S. Ahn, D. Beljonne, J. L. Bredas, C. J. Bardeen, and F. C. Spano (unpublished).
[47] M. R. Philpott, J. Chem. Phys. **55**, 2039 (1971).
[48] M. Hoffmann and Z. G. Soos, Phys. Rev. B **66**, 024305/1 (2002).
[49] G. C. Morris and M. G. Sceats, Chem. Phys. **3**, 164 (1974).
[50] L. B. Clark and M. R. Philpott, J. Chem. Phys. **53**, 3790 (1970).
[51] A. R. Lacey and L. E. Lyons, Proc. Chem. Soc., London, 414 (1960).
[52] J. A. Gisby and S. H. Walmsley, Chem. Phys. **122**, 271 (1988).
[53] J. Ferguson, Z. Phys. Chem. (Munich) **101**, 45 (1976).
[54] V. M. Agranovich and V. L. Ginzburg, *Crystal Optics with Spatial Dispersion, and Excitons* (Springer-Verlag, Heidelberg, 1984).
[55] V. M. Agranovich, O. A. Dubovsky, K. I. Grigorishin, T. A. Leskova, T. Neidlinger, and P. Reineker, Chem. Phys. **203**, 11 (1996).
[56] J. B. Birks and J. W. Cameron, Proc. R. Soc. London, Ser. A **249**, 297 (1959).
[57] J. B. Birks, *Photophysics of Aromatic Molecules* (Wiley, London, 1970).
[58] H. Shimura and Y. Ohba, Jpn. J. Appl. Phys. **20**, 1683 (1981).
[59] B. J. Mulder, J. Phys. Chem. Solids **29**, 182 (1967).
[60] M. Tomura and Y. Takahashi, J. Photogr. Sci. **25**, 647 (1968).
[61] A. G. Bale, J. Bridge, and D. B. Smith, Chem. Phys. Lett. **42**, 166 (1976).
[62] R. N. Ahmad-Bitar, B. R. Bulos, I. R. Hassan, and M. H. Jomah, Jpn. J. Appl. Phys., Part 1 **25**, 583 (1986).
[63] G. C. Morris, S. A. Rice, and A. E. Martin, J. Chem. Phys. **52**, 5149 (1970).
[64] W. Helfrich and F. R. Lipsett, J. Chem. Phys. **43**, 4368 (1965).
[65] E. A. Chandross, J. Ferguson, and E. G. McRae, J. Chem. Phys. **45**, 3546 (1966).
[66] L. E. Lyons and L. J. Warren, Aust. J. Chem. **25**, 1411 (1972).
[67] J. B. Birks, Mol. Cryst. Liq. Cryst. **28**, 117 (1974).
[68] J. O. Williams, B. P. Clarke, J. M. Thomas, and M. J. Shaw, Chem. Phys. Lett. **38**, 41 (1976).
[69] J. O. Williams and B. P. Clarke, J. Chem. Soc., Faraday Trans. 2 **73**, 1371 (1977).
[70] D. P. Craig and J. Rajikan, J. Chem. Soc., Faraday Trans. 2 **74**, 292 (1978).
[71] Y. Takahashi, K. Uchida, and M. Tomura, J. Lumin. **15**, 293 (1977).
[72] R. Horiguchi, N. Iwasaki, and Y. Maruyama, J. Phys. Chem. **91**, 5135 (1987).
[73] E. A. Silinsh, *Organic Molecular Crystals. Their Electronic States* (Springer-Verlag, Berlin, 1980).
[74] P. E. Fielding and R. C. Jarnagin, J. Chem. Phys. **47**, 247 (1967).
[75] S. A. Rice, G. C. Morris, and W. L. Greer, J. Chem. Phys. **52**, 4279 (1970).
[76] V. A. Lisovenko, M. T. Shpak, and V. G. Antoniuk, Chem. Phys. Lett. **42**, 339 (1976).
[77] X. H. Sun, Z. Zhao, F. C. Spano, D. Beljonne, J. Cornil, Z. Shuai, and J. L. Bredas, Adv. Mater. (Weinheim, Ger.) **15**, 818 (2003).
[78] S. L. Murov, I. Carmichael, and G. L. Hug, *Handbook of Photochemistry*, 2nd ed. (Dekker, New York, 1993).
[79] D. Mobius and H. Kuhn, J. Appl. Phys. **64**, 5138 (1988).